Nanoscale Advances

ROYAL SOCIETY OF CHEMISTRY

PAPER

View Article Online
View Journal | View Issue

Check for updates

Cite this: *Nanoscale Adv.*, 2025, **7**, 4740

Generation of optical frequency combs in optically injected integrated gain-switched semiconductor lasers and their applications in Doppler LIDAR

Yunshan Zhang,[a] Yibing Chen,[a] Mengxi Zhou,[a] Yitong Liu,[b] Wenxuan Ma,[a] Zeyu Gang,[b] Zhenxing Sun,[b] Jilin Zheng,*[c] Xiangfei Chen[b] and Pu Li*[d]

Received 19th March 2025
Accepted 15th June 2025

DOI: 10.1039/d5na00260e

rsc.li/nanoscale-advances

This paper introduces an optical frequency comb (OFC) source. It is constructed using a monolithically integrated gain-switched semiconductor laser with the optical injection technique. The theoretical analysis of the working principle of this integrated OFC source based on optical injection is carried out. Fabricated *via* micro–nano processing technology, the proposed OFC source has been experimentally investigated. The results clearly show that the optical injection method can notably increase the number of comb teeth with a higher carrier-to-noise ratio. The measured phase noise of the beat-frequency signal between comb teeth is less than −102 dBc Hz^{-1} @ 10 kHz. Moreover, a Doppler velocity-measuring LIDAR system is designed based on this OFC source, and the velocity of a moving target is measured. Compared with single-frequency speed measurement, using multi-comb teeth for speed measurement can significantly reduce the error.

Open Access Article. Published on 17 June 2025. Downloaded on 5/1/2026 6:40:59 AM. This article is licensed under a Creative Commons Attribution-NonCommercial 3.0 Unported Licence.

1 Introduction

Optical frequency combs (OFCs) have a wide range of applications in optical communication, spectroscopy, optical atomic clocks, microwave photonics, and light detection and ranging (LIDAR).[1–5] There are several methods that can generate OFCs, such as mode-locked lasers, Kerr-comb generation *via* nonlinear effects, OFCs based on external electro-optic modulations, OFCs generated by quantum cascade lasers and gain-switched OFCs.[6–12] For mode-locked laser-based OFCs, the comb tooth spacing is fundamentally determined by the laser cavity length, creating a fixed frequency grid that is inherently difficult to tune dynamically. This rigidity poses challenges in applications requiring reconfigurable frequency spacing, such as adaptive spectroscopic analysis or flexible optical communication protocols. Kerr-comb generation in high-Q microresonators has emerged as a compact alternative, leveraging nonlinear optical effects to generate dense frequency combs from a single continuous-wave laser. However, this approach critically relies on ultra-high-quality-factor microresonators (*e.g.*, silicon nitride or silicon structures), which demand nanoscale fabrication precision and rigorous thermal stability control. Additionally, the dense mode spacing in high-Q cavities can lead to mode competition and phase noise challenges, requiring sophisticated optical feedback mechanisms to stabilize comb coherence. OFCs based on external electro-optic modulations offer tunable comb spacing through external electrical modulation of a laser's phase or amplitude. This flexibility makes them suitable for applications requiring frequency agility, such as microwave photonics and dual-comb spectroscopy. However, this approach is hindered by inherent limitations: high insertion losses from the modulator itself reduce optical power efficiency, while the bandwidth of the comb is constrained by the frequency response of the electro-optic device. The gain switching (GS) technique for generating optical frequency combs has attracted extensive attention due to its advantages such as flexible selection of frequency intervals, compact structure, low power consumption, and ease of implementation.[12,13] The GS technique involves driving a semiconductor laser using a radio-frequency (RF) signal. This RF signal, typically sinusoidal in nature, is superimposed onto a direct bias current. Under this dual-signal drive, the semiconductor laser enters a periodic switch-off state, enabling it to generate short optical pulses at regular intervals. In the optical spectrum, a series of equidistantly spaced spectral lines emerges, characteristic of the gain-switched operation mode. Traditional gain-switched optical frequency combs (GS-OFCs) suffer from several limitations. Prominently, they exhibit a relatively small number of comb teeth, and their carrier-to-noise ratio (CNR) is rather poor.[14] This restricts their

[a]*College of Electronic and Optical Engineering and College of Flexible Electronics (Future Technology), Nanjing University of Posts and Telecommunications, Nanjing 210023, China. E-mail: yszhang@njupt.edu.cn*

[b]*College of Engineering and Applied Sciences, Nanjing University, Nanjing 210023, China*

[c]*College of Communications Engineering, PLA Army Engineering University, Nanjing 210007, China. E-mail: zhengjilinjs@126.com*

[d]*Guangdong Provincial Key Laboratory of Photonics Information Technology, School of Information Engineering, Guangdong University of Technology, Guangzhou 510006, China. E-mail: lipu@gdut.edu.cn*

© 2025 The Author(s). Published by the Royal Society of Chemistry

Open Access Article. Published on 17 June 2025. Downloaded on 5/1/2026 6:40:59 AM. This article is licensed under a Creative Commons Attribution-NonCommercial 3.0 Unported Licence.

performance and applications in scenarios where high-precision and high-quality spectral characteristics are required. Research has proven that the optical injection technique can effectively increase the number of comb teeth and improve the spectral quality of optical frequency combs.[15,16] Unfortunately, the optical injection technique typically relies on discrete components for implementation. This leads to a system that is not only large in size but also highly vulnerable to external interference, rendering it extremely challenging to achieve practical applications.[17]

This paper theoretically and experimentally demonstrates a monolithically integrated GS-OFC based on the optical injection technique. The operating principle of the integrated GS-OFC employing the optical injection technique is analyzed using the time-domain traveling-wave method. Furthermore, the proposed GS-OFC chip is fabricated utilizing a micro–nano-processing technology called the reconfigurable-equivalent-chirping (REC) technique.[18–20] The output characteristics of the GS-OFC chip are experimentally studied in detail. The experimental results show that the number of comb teeth within the 10 dB bandwidth range is increased from 9 to 24 and the CNR of the OFCs is enhanced from 19.9 dB to 30.7 dB by the optical injection method. Drawing on the reported GS-OFC source, we devised an initial Doppler LIDAR velocimetry system and carried out target velocity-measurement experiments. Experimental findings indicate that, with the optical frequency comb having multiple frequency comb teeth, each tooth can acquire the target's velocity information during each measurement. Employing the averaging method, the velocity-measurement accuracy of the system can be enhanced remarkably.

2 Operating principles

Based on the transfer matrix, in order to further analyze the dynamic characteristics of the laser, the rate equation of laser carriers can be incorporated to solve the coupled wave equations in the time domain. This method is called the distributed time-domain traveling-wave method (TDM).[21,22] The schematic diagram of the TDM is shown in Fig. 1. Utilizing the TDM method, a laser with a cavity length of L is divided into N microelements, and the length of a single microelement is Δz, and the time for light to pass through a single microelement is Δt. In unit time, the parameters of each microelement can be assigned independently. If the length of the microelement is sufficiently small, the carrier density distribution and photon density distribution within these microelements can be considered uniform, which is suitable for analyzing the operating characteristics of the proposed integrated GS-OFC laser chip.

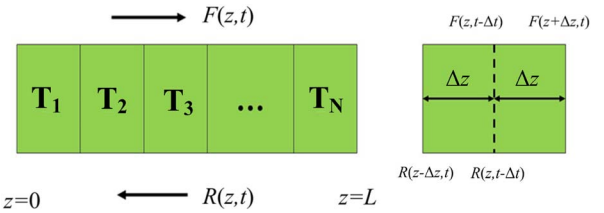

Fig. 1 Schematic diagram of the TDM.

The electromagnetic field inside the laser chip can be expressed as:

$$E(x,y,z,t) = \phi(x,y)[F(z,t)e^{-i\beta_0 z} + R(z,t)e^{i\beta_0 z}]e^{i\omega_0 z} \quad (1)$$

where $\phi(x,y)$ is the modal distribution within the cross-section of the laser waveguide. $F(z,t)$ and $R(z,t)$ represent the forward-propagating component and the backward-propagating component of the electromagnetic field, respectively. β_0 and ω_0 are the propagation constant and angular frequency at the Bragg wavelength (λ_0), respectively. The $F(z,t)$ and $R(z,t)$ satisfy the time-dependent coupled wave equations.

$$\frac{1}{c_g}\frac{\partial F(z,t)}{\partial t} + \frac{\partial F(z,t)}{\partial z} = (G - i\delta)F(z,t) + i\kappa R(z,t) + s_f(z,t) \quad (2)$$

$$\frac{1}{c_g}\frac{\partial R(z,t)}{\partial t} + \frac{\partial R(z,t)}{\partial z} = (G - i\delta)R(z,t) + i\kappa^* R(z,t) + s_r(z,t) \quad (3)$$

c_g is the group velocity of the electromagnetic field. G and δ represent the modal amplitude gain and detuning factor. $s_f(z,t)$and $s_r(z,t)$ are the spontaneous emission noises of the forward transmission component and the backward transmission component, respectively. Laser oscillation originates from spontaneous emission noise, meaning that spontaneous emission noise serves as the driving source for the formation of laser oscillation. Therefore, $s_f(z,t)$ and $s_r(z,t)$ in eqn (2) and (3) serve as the initial conditions for the equations. The amplitude distributions of $s_f(z,t)$ and $s_r(z,t)$ are set to follow a Gaussian distribution, and their phases are assumed to vary randomly. During the solution of the equations, $s_f(z,t)$ and $s_r(z,t)$ are generated by a random number generator that conforms to a Gaussian distribution. More detailed descriptions of the spontaneous emission noise can be found in ref. 21 and 22.

κ is the coupling coefficient and is expressed as:

$$\kappa = \kappa_i + i\kappa_g \quad (4)$$

κ_i is the refractive index coupling coefficient, and k_g is the gain coupling coefficient. Based on Taylor expansion, $F(z,t)$ and $R(z,t)$ can be represented in matrix form as:

$$\begin{pmatrix} F(z+\Delta z,t) \\ R(z-\Delta z,t) \end{pmatrix} = \begin{pmatrix} \mathrm{sech}(\gamma\Delta z) & i\tanh(\gamma\Delta z) \\ i\tanh(\gamma\Delta z) & \mathrm{sech}(\gamma\Delta z) \end{pmatrix} \begin{pmatrix} \exp\{(G-i\delta)\Delta z & 0 \\ 0 & \exp\{(G-i\delta)\Delta z \end{pmatrix} \begin{pmatrix} F(z,t-\Delta t) \\ R(z,t-\Delta t) \end{pmatrix} \quad (5)$$

where $\gamma = \sqrt{\kappa\kappa^*}$.

Open Access Article. Published on 17 June 2025. Downloaded on 5/1/2026 6:40:59 AM. This article is licensed under a Creative Commons Attribution-NonCommercial 3.0 Unported Licence.

The gain in each microelement can be expressed as:

$$G(z,t) = \frac{\Gamma g \ln(N(z,t)/N_0)}{2(1+\varepsilon P(z,t))} - \frac{\alpha}{2} \quad (6)$$

where Γ is the optical confinement factor, g is the gain coefficient, N_0 is the transparent carrier density, ε is the gain saturation coefficient, α is the internal waveguide loss caused by scattering and inter-valence band absorption, and $P(z,t)$ is the photon density.

$$P(z,t) = |F(z,t)|^2 + |R(z,t)|^2 \quad (7)$$

$$\delta = \frac{\omega_0}{c}\left(n_{\mathrm{eff},0} + \Delta n\right) - \frac{\pi}{\Lambda_0} \quad (8)$$

$$\Delta n = -\frac{\lambda_0}{4\pi}\Gamma \alpha_{\mathrm{m}} \ln(N(z,t)/N_0) \quad (9)$$

c is the speed of light in a vacuum, $n_{\mathrm{eff},0}$ is the effective refractive index of the waveguide under transparent current, Δn is variation of the refractive index caused by carrier density fluctuations, Λ_0 is the grating period, α_{m} is the material linewidth enhancement factor, and N_0 is the transparent carrier density. The carrier density can be expressed as:

$$\frac{\mathrm{d}N}{\mathrm{d}t} = \frac{I}{ed_{\mathrm{act}}} - AN(z,t) - BN(z,t)^2 - CN(z,t)^3 - \frac{v_g g \ln\left(\frac{N(z,t)}{N_0}\right)P(z,t)}{1+\varepsilon P(z,t)} \quad (10)$$

I is the current density, d_{act} is the thickness of the active layer, and A, B, and C are the linear recombination coefficient, the spontaneous recombination coefficient, and the Auger recombination coefficient respectively, g is the gain coefficient. Under the GS state, the current density will be modulated by an external RF signal:

$$I(t) = I_0 + I_{\mathrm{a}} \sin(2\pi f_{\mathrm{m}} t) \quad (11)$$

where I_0 is the bias current, I_{a} is the modulation amplitude, and f_{m} is the modulation frequency.

When using the TDM method to solve the output characteristics of a laser, it is also necessary to determine the boundary conditions. The left facet of the laser is defined at $z = 0$, where the facet boundary conditions for the forward and reverse traveling waves are satisfied by:

$$\begin{cases} F(0,t) = r_{\mathrm{l}} R(0,t) \\ R(L,t) = r_{\mathrm{r}} F(L,t) \end{cases} \quad (12)$$

r_{l} and r_{r} are the reflectivities of the left-hand and right-hand end faces of the laser respectively.

The structure of the GS-OFC laser and its grating are shown in Fig. 2. It consists of two back-to-back DFB laser sections (*i.e.*, DFB1 and DFB2). The cavity lengths of the two DFB lasers are labeled as L_1 and L_2. DFB1 and DFB2 are biased by currents of I_1 and I_2 respectively, and DFB2 is modulated by a RF signal simultaneously. In the monolithic integrated optical injection state, we usually refer to the RF modulated laser as the slave laser, and refer to the other one as the master laser. As shown in

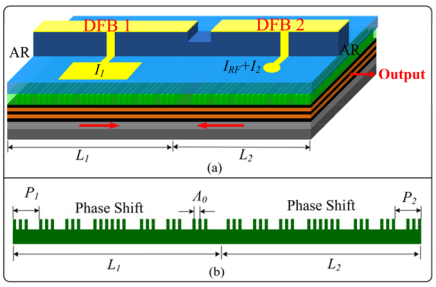

Fig. 2 (a) Schematic of the GS-OFC laser chip, (b) structure of the grating in the GS-OFC laser chip.

Fig. 2(b), both of the gratings in the two DFB lasers are designed by the REC technique with the identical seed grating period Λ_0. In order to obtain high single-longitudinal mode (SLM) yield, equivalent phase shifts are employed in the gratings. The wavelengths of the lasers are determined by the sampling periods P_1 and P_2. Through tuning the sampling periods, the wavelengths of the two DFB lasers and the detuning frequency can be controlled accurately,[23] which is sufficient for the GS-OFC laser.

In integrated two-section distributed feedback (DFB) laser chips, varying the injection currents to DFB1 and DFB2 induces a series of dynamic nonlinear phenomena, including four-wave mixing (FWM), double-periodic oscillation, quasi-periodic oscillation, and chaotic behaviors. Among these, FWM,

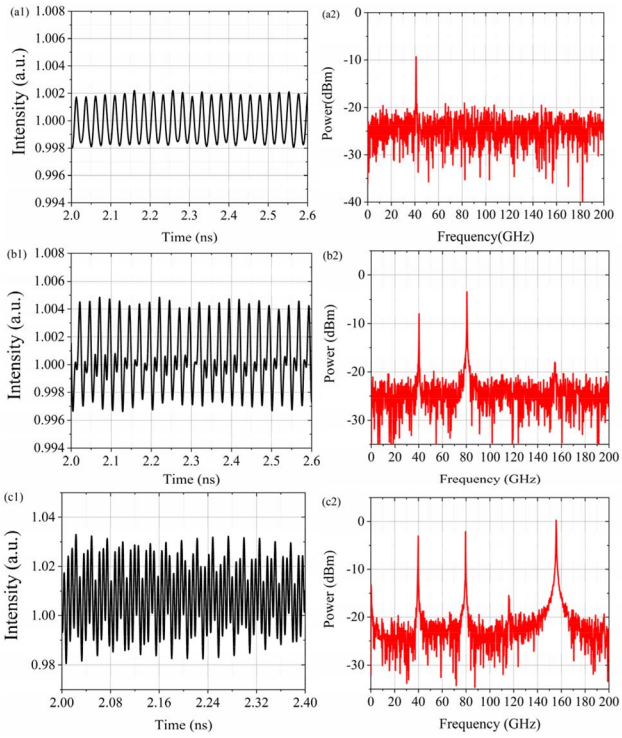

Fig. 3 The optical intensity time series and their frequency spectra of the laser under different states. (a1) and (a2) correspond to FWM, (b1) and (b2) correspond to double-periodic oscillations, (c1) and (c2) correspond to under quasi-periodic oscillations.

© 2025 The Author(s). Published by the Royal Society of Chemistry

Open Access Article. Published on 17 June 2025. Downloaded on 5/1/2026 6:40:59 AM.
This article is licensed under a Creative Commons Attribution-NonCommercial 3.0 Unported Licence.

Table 1 The main parameters used in the simulation of the GS-OFC laser

Parameters	Symbol	Values
Length of section I	L_1	350 μm
Length of section II	L_2	450 μm
Period of the seed grating	Λ_0	252.03 nm
Sampling period of DFB1	P_1	5 μm
Sampling period of DFB2	P_2	4.968 μm
Equivalent coupling coefficient	κ	30 cm^{-1}
Effective refractive index at transparency	$n_{eff,0}$	3.23
Group refractive index	n_g	3.6
Linear recombination coefficient	A	1×10^{9} s^{-1}
Bimolecular recombination coefficient	B	1×10^{-10} cm^3 s^{-1}
Auger recombination coefficient	C	7.5×10^{-29} cm^6 s^{-1}
Spontaneous coupling factor	β	2.5×10^{-5}
Gain coefficient	g	1100 cm^{-1}
Waveguide loss	α	10 cm^{-1}
Confinement factor	Γ	0.1
Gain compression factor	ε	4×10^{-17} cm^3
Linewidth enhancement factor	α_H	2
Transparency carrier density	N_0	1×10^{18} cm^{-3}

double-periodic, and quasi-periodic oscillations are critical for expanding the spectral bandwidth of gain-switched optical frequency combs. Fig. 3 illustrates the optical intensity time series and their frequency spectra of the laser calculated using the TDM under FWM, double-periodic, and quasi-periodic oscillation conditions without RF modulation. Notably, in the FWM regime, the optical intensity time series of the laser contains only a single-frequency component, demonstrating enhanced coherence between the two laser sections. This characteristic significantly promotes the improvement of gain-switched optical frequency comb quality, highlighting the advantages of FWM-based operation for generating high-fidelity frequency combs.

Utilizing the TDM method, the output characteristics of the proposed GS-OFC laser can be demonstrated. The main parameters used in the simulation are shown in Table 1. Firstly, the current of DFB1 is set to 0, and the current of DFB2 is set to 50 mA. The GS effect of the free-running laser under different modulation conditions is investigated. Fig. 4 shows the laser spectrum and the corresponding time-domain signal obtained at different modulation intensities when the modulation signal frequency is 10 GHz. When the modulation current of the laser is 10 mA, the laser is in the small-signal modulation state, and there is no gain-switching effect, and no comb teeth can be observed in the spectrum. When the modulation current increases to 50 mA, the laser exhibits the gain-switching effect, pulses appear in the time-domain signal of the laser, and multiple comb teeth appear in the spectrum. The number of comb teeth within the 10 dB bandwidth range is 5. When the modulation current is further increased to 100 mA, the GS effect of the laser becomes more pronounced, and the number of comb teeth increases to 7.

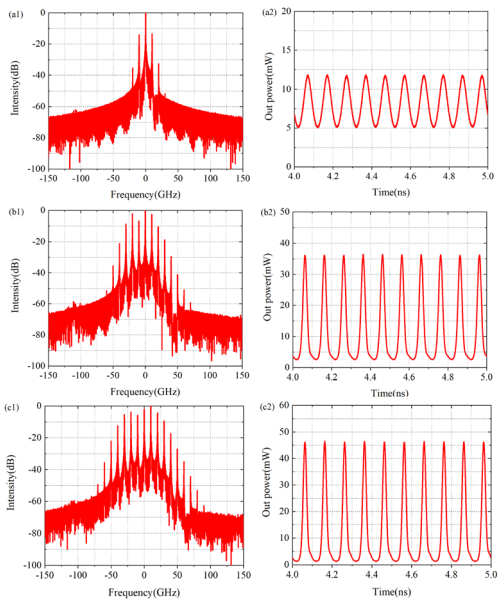

Fig. 4 The simulated spectra of the GS-OFC at different RF currents when a 10 GHz RF signal is injected. (a1) and (a2) $I_{RF} = 10$ mA, (b1) and (b2) $I_{RF} = 50$ mA, (c1) and (c2) $I_{RF} = 100$ mA.

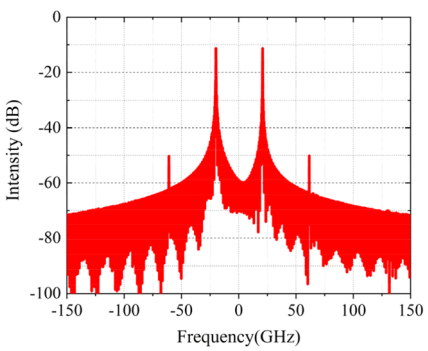

Fig. 5 The simulated spectrum of the GS-OFC laser under the FWM state.

Open Access Article. Published on 17 June 2025. Downloaded on 5/1/2026 6:40:59 AM. This article is licensed under a Creative Commons Attribution-NonCommercial 3.0 Unported Licence.

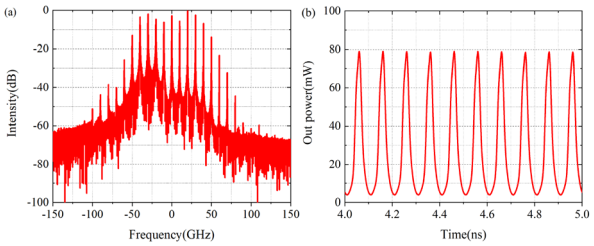

Fig. 6 (a) The simulated spectrum of the GS-OFC under FWM state when DFB2 is modulated by the 10 GHz RF signal with 100 mA current, and (b) the simulated corresponding time-domain signal of the GS-OFC.

In order to improve the quality of the OFC, the optical injection technique is employed. The injection current of DFB2 is kept constant at 50 mA and the injection current of DFB1 is increased. When the current of DFB1 is increased to 50 mA, the four-wave mixing (FWM) effect occurs within the laser chip. The spectrum of the laser under the FWM state is shown in Fig. 5. Meanwhile, if an RF signal is injected into DFB2, OFCs will be generated. The spectrum and the corresponding time-domain signal of the GS-OFC are shown in Fig. 6, when DFB2 is modulated by a 10 GHz RF signal with a current of 100 mA. It can be seen that the number of comb teeth within the 10 dB bandwidth range increases significantly.

3 Design and fabrication of the laser chip

The fabrication process of the GS-OFC laser chip utilizing the REC technique is shown in Fig. 7. First, an n-InAlGaAs lower optical confinement layer, an InAlGaAs multiple quantum well structure, a p-InAlGaAs upper optical confinement layer, and a p-InGaAsP grating layer are successively grown on the wafer by conventional metal–organic chemical vapor deposition (MOCVD). A uniform grating is created on the grating layer using holographic exposure technology. Then, a micro–nano sampled grating structure is fabricated on the basis of the uniform grating by means of ordinary photolithography. Fig. 8(b) is the scanning electron microscopy (SEM) image of the sampling grating of the laser. The period of the uniform grating Λ_0 is determined by the holographic exposure process with

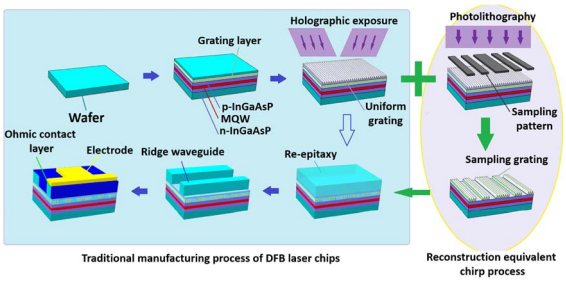

Fig. 7 The micro–nano fabrication process of the GS-OFC laser chip based on the REC technique.

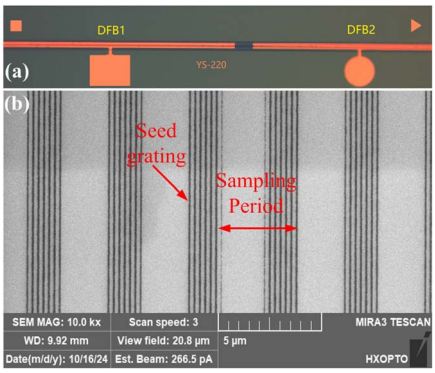

Fig. 8 (a) Photograph of the GS-OFC laser chip and (b) SEM of the sampled gratings in the GS-OFC laser chip.

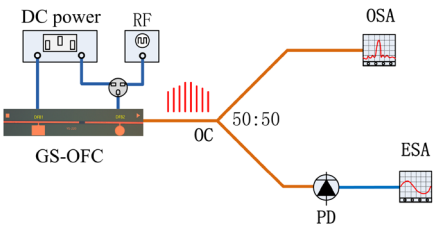

Fig. 9 Schematic diagram of the experimental setup (OC: optical coupler, PD: photo-detector, OSA: optical spectrum analyser, ESA: electrical signal analyser.).

a precision of ±3 pm and the sampling periods (P_1 and P_2) of the sampled grating are determined by the lithography pattern. After forming the sampled grating, a p-InP cladding layer and a p-InGaAs contact layer are successively regrown over the entire structure. The devices are realized by processing ridge waveguides, opening p-metal contact windows, followed by metallization. In addition, in order to obtain high electrical isolation, a small area of the highly p-doped InGaAs contact layer between the two sections is removed by etching. Finally, AR coatings with reflectivity less than 1% are deposited on both facets to suppress the Fabry–Perot modes of the lasers. Fig. 8(a) is the photograph of the developed GS-OFC laser chip. The cavity lengths of the DFB1 and DFB2 chips are 450 μm and 350 μm respectively. The wavelength difference between them is set at 0.4 nm.

4 Experimental results

The schematic diagram of the experimental system is shown in Fig. 9. DFB1 and DFB2 are biased by a DC power supply. The RF signal modulates the DFB2 laser through a bias tee. The laser light is split into two beams by a 50 : 50 optical coupler (OC). One beam is transmitted to a high-resolution optical spectrum analyzer (OSA), and the other beam is sent through a photodetector (PD) to an electrical signal analyzer (ESA) for the detection of the beat-frequency signal between the OFCs.

Fig. 10 shows the spectrum of the laser when the injection currents of DFB1 and DFB2 are 55 mA and 70 mA, respectively.

© 2025 The Author(s). Published by the Royal Society of Chemistry

Open Access Article. Published on 17 June 2025. Downloaded on 5/1/2026 6:40:59 AM. This article is licensed under a Creative Commons Attribution-NonCommercial 3.0 Unported Licence.

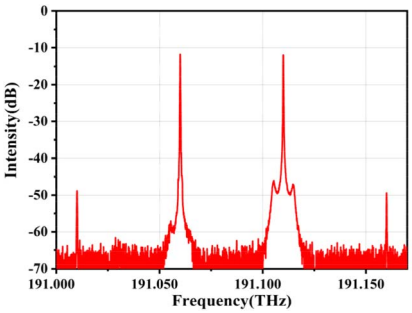

Fig. 10 The measured spectrum of the GS-OFC under the FWM state.

It can be seen that the laser is in the four-wave mixing (FWM) state at this time. Fig. 11 presents the spectra of the GS-OFC laser under the modulation of a 3 GHz RF signal in the free-running and FWM states. In the free-running state, DFB2 is biased at a current of 55 mA, while DFB1 has no bias current (*i.e.*, the bias current of DFB1 is 0). The number of comb teeth within the 10 dB bandwidth range is 9 in the free running state, while the number increases to 24 in the FWM state. Due to the optical injection technique, the CNR of the optical frequency comb increases from 19.9 dB to 30.7 dB, which implies higher coherence.

When the frequency of the radio-frequency (RF) signal varies, the spectrum of the optical frequency comb (OFC) changes accordingly. Fig. 12 presents the optical spectra of the GS-OFC with the RF signal frequency set at 4 GHz and 8 GHz, respectively. As the RF signal frequency changes, the range of the laser's OFC shows no significant variation. Phase noise is one of the most important figures of merit for OFCs. Fig. 13 depicts the phase noise spectra of the beat-frequency signal between the OFCs, measured when the RF signal frequencies are 4 GHz and 8 GHz, respectively. It can be observed that when the frequency of the modulated RF signal is altered from 4 GHz to 8 GHz, the phase noise of the beat-frequency signal remains nearly

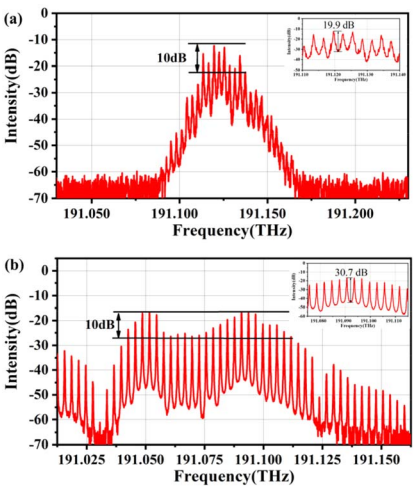

Fig. 11 (a) The measured spectrum of the OFC in the free running state, and (b) the measured spectrum of the OFC in the FWM state.

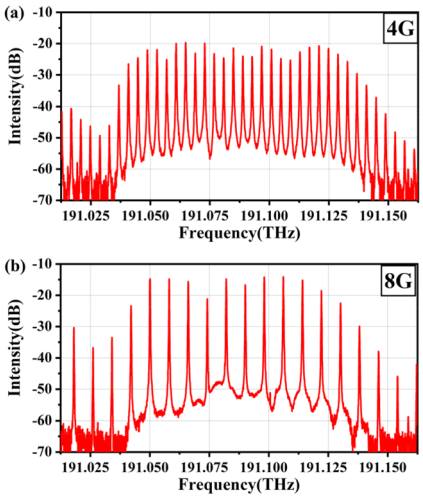

Fig. 12 (a) Optical spectra of the GS-OFC with the RF signal frequency set at 4 GHz; (b) optical spectra of the GS-OFC with the RF signal frequency set at 8 GHz.

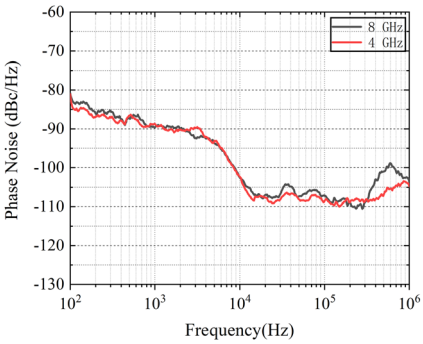

Fig. 13 Phase noise spectra of the GS-OFC laser when the RF is set at 4 GHz and 8 GHz.

unchanged, being 102.22 dBc Hz^{-1} and 102.9 dBc Hz^{-1} at a frequency offset of 10 kHz, respectively.

Stability is one of the important figures of merit for optical frequency combs. Fig. 14(a) shows the variation in the phase noise of the proposed GS-OFC at a frequency offset of 10 kHz at 25 °C over one hour, and Fig. 14(b) shows the statistical results of the phase noise. It can be seen that the average value of the phase noise is −102 dBc Hz @10 kHz with a standard deviation of 0.599 dBc Hz^{-1}. Fig. 15 shows the measured phase noise of the GS-OFC at different temperatures. The measured results show that the phase noise of the GS-OFC increases slightly as the temperature rises, with the maximum phase noise reaching −102.02 dBc Hz^{-1} @10 kHz at 40 °C. Overall, the phase noise of the proposed GS-OFC can maintain high stability, which is beneficial for improving the coherence detection accuracy in Doppler velocity measurement.

A proof-of-concept Doppler velocity measurement system is designed based on the proposed GS-OFC source, and is shown in Fig. 16. The light from the GS-OFC source is split into two beams by an optical coupler (OC1). The first beam is directed into another optical coupler (OC2) as the reference signal. The

© 2025 The Author(s). Published by the Royal Society of Chemistry

Open Access Article. Published on 17 June 2025. Downloaded on 5/1/2026 6:40:59 AM.
This article is licensed under a Creative Commons Attribution-NonCommercial 3.0 Unported Licence.

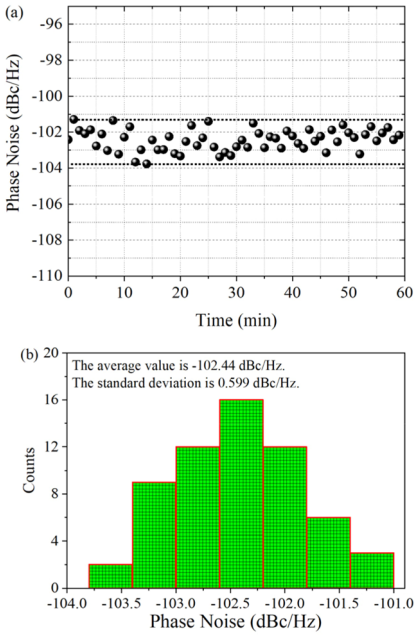

Fig. 14 (a) Variation of the GS-OFC phase noise during one hour, and (b) the statistical values of the GS-OFC phase noise during one hour.

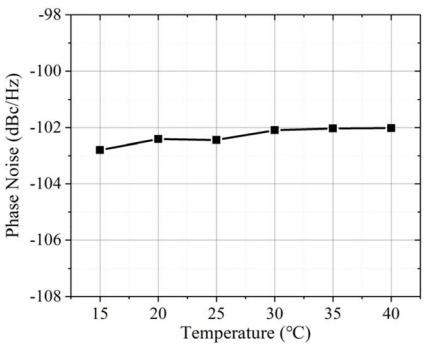

Fig. 15 The variation of the GS-OFC phase noise with temperature.

second beam is sent to the port 1 of an optical circulator as the probe signal, then transmitted through a collimator, and finally reflected by the target. The back-reflected light is then mixed with the reference signal in the OC2 and detected by a balanced photodetector (BPD). The detected electrical signal is acquired by a data acquisition card (DAC) and digital frequency mixed

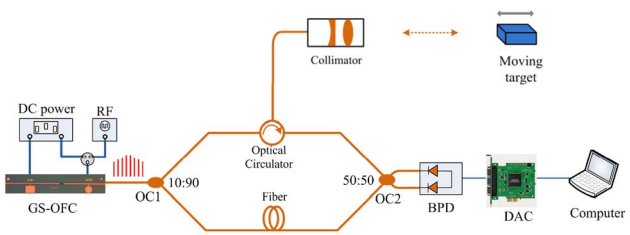

Fig. 16 Schematic diagram of the Doppler velocity measurement system.

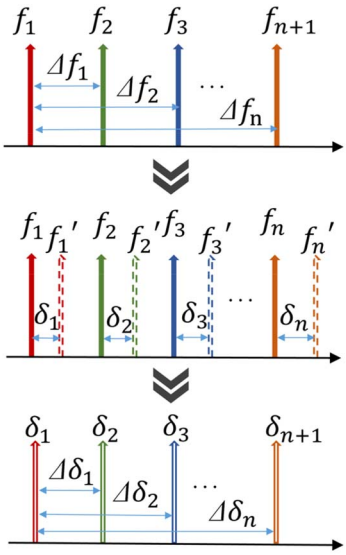

Fig. 17 Principle of the Doppler velocimetry based on the OFC.

and analyzed by a computer. By conducting Fourier transform in the digital domain, we are able to retrieve the frequency of the electrical signal.

The Doppler velocimetry principle based on an OFC is presented in Fig. 17. The frequencies corresponding to each comb-tooth are denoted as $f_1, f_2 \ldots f_n, f_{n+1}$. The frequency differences are expressed as $\Delta f_n = f_{n+1} - f_1$. When the laser impinges on a moving object, a Doppler shift is induced for each frequency. Consequently, these frequencies transform into $f_1', f_2' \ldots f_n', f_{n+1}'$ and the Doppler shift generated for each frequency is defined as $\delta_n = f_n' - f_n$. The relationship between the Doppler shifts of diverse frequencies and the velocity of the object can be

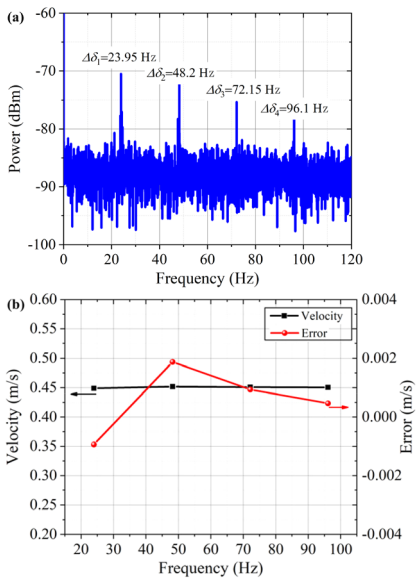

Fig. 18 (a) Spectrum of the measured signal with the target speed of 0.45 m s^{-1} and the comb tooth interval of 8 GHz, and (b) the measured target speeds and errors utilizing different comb teeth.

© 2025 The Author(s). Published by the Royal Society of Chemistry

Open Access Article. Published on 17 June 2025. Downloaded on 5/1/2026 6:40:59 AM. This article is licensed under a Creative Commons Attribution-NonCommercial 3.0 Unported Licence.

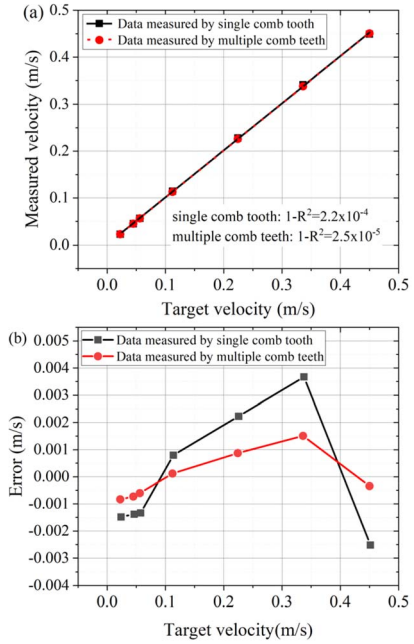

Fig. 19 (a) Measured target velocities employing a single comb tooth and multiple comb teeth of the OFC, (b) measurement errors employing a single comb tooth and multiple comb teeth of the OFC.

mathematically expressed as $\delta_1 = 2vf_1/c$, $\delta_2 = 2vf_2/c \ldots \delta_n = 2vf_n/c$. From these relationships, the velocity of the target can be obtained as:

$$v = \frac{c\Delta\delta_n}{2\Delta f_n} \tag{13}$$

where $\Delta\delta_n = \delta_{n+1} - \delta_1$.

Fig. 18(a) shows the spectrum of the measured signal when the target speed is set to 0.45 m s^{-1} and the comb tooth interval is 8 GHz. Fig. 18(b) presents the target speed calculated according to formula (13) and the measurement error. The maximum error of the target speed measured by using a single comb tooth is 0.0019 m s^{-1}. The speed obtained by averaging the target speeds measured using different comb teeth is 0.4506 m s^{-1}. The measurement error is reduced to 0.0006 m s^{-1}.

Fig. 19 presents the target velocities and measurement errors derived from tests employing a single comb tooth and multiple comb teeth of the OFC. In Fig. 19(a), we compare the experimental results with the set velocities and conduct a linear fitting analysis on the data. It is evident that for the data obtained using multiple comb teeth, the $1 - R^2$ factor after fitting decreases from 2.2×10^{-4} to 2.5×10^{-5}, thus enhancing the velocity measurement accuracy. Fig. 19(b) depicts the measured errors at various speeds. Notably, the multi-comb-tooth measurement method reduces the maximum error from 0.0053 m s^{-1} to 0.0026 m s^{-1}.

5 Conclusions

This paper reports a monolithically integrated GS-OFC source based on optical injection technology. The output characteristics of the monolithically integrated GS-OFC are investigated both theoretically and experimentally. The research results show that the optical injection technology can effectively increase the number of comb teeth and the CNR of the GS-OFC. In addition, a Doppler velocity measurement experiment is carried out based on the reported OFC source. The velocity measurement results indicate that the use of the OFC can effectively improve the accuracy of velocity measurement.

Data availability

The data supporting the findings of this study are available within the article.

Author contributions

Y. Zhang conceived the idea of this study. Y. Chen, W. Ma and M. Zhou performed the measurements and analysed the data. Z. Gang, Y. Liu, Z. Sun, and J. Zheng fabricated the devices. Y. Zhang, X. Chen and P. Li contributed to the data analysis. Y. Zhang, J. Zheng and P. Li wrote and revised the manuscript. All authors participated in the manuscript preparation.

Conflicts of interest

There are no conflicts to declare.

Acknowledgements

This research was partially supported by the National Natural Science Foundation of China, under grant numbers 62374092, 62371470 and 62404098; in part by the Key Research and Development Program of Jiangsu Province, under grant number BE2023083; in part by the Natural Science Foundation of Jiangsu Province of China, under Grant BK20241196.

References

1 P. Marin-Palomo, J. N. Kemal and M. Karpov, *Nature*, 2017, **546**, 274–279.
2 J. Ye, H. Schnatz and L. W. Hollberg, *IEEE J. Sel. Top. Quantum Electron.*, 2003, **9**, 1041–1058.
3 K. Beloy, M. I. Bodine and T. Bothwell, *Nature*, 2021, **591**, 564–569.
4 J. Liu, E. Lucas and A. S. Raja, *Nat. Photonics*, 2020, **14**, 486–491.
5 I. Coddington, W. Swann and L. Nenadovic, *Nat. Photonics*, 2009, **3**, 351–356.
6 H. A. Haus, *IEEE J. Sel. Top. Quantum Electron.*, 2000, **6**, 1173–1185.
7 T. J. Kippenberg, A. L. Gaeta, M. Lipson and M. L. Gorodetsky, *Science*, 2018, **361**, eaan8083.
8 A. Parriaux, K. Hammani and G. Millot, *Adv. Opt. Photon*, 2020, **12**, 223–287.
9 Z. P. Li, X. H. Ma, K. Zhou, B. B. Liu, C. J. Wang, X. Y. Liao, W. Guan, S. M. Wu, H. Liu, Z. Z. Zhang, J. C. Cao, M. Li,

Open Access Article. Published on 17 June 2025. Downloaded on 5/1/2026 6:40:59 AM.
This article is licensed under a Creative Commons Attribution-NonCommercial 3.0 Unported Licence.

M. Yan, H. P. Zeng and H. Li, *Laser Photonics Rev.*, 2023, **17**, 2200418.
10 G. B. Liu, X. H. Ma, K. Zhou, B. B. Liu, L. L. Zheng, X. L. Bi, S. M. Wu, Y. M. Lu, Z. P. Li, W. J. Wan, Z. Z. Zhang, J. S. Peng, Y. Zhang, H. P. Zeng and H. Li, *Light Sci. Appl.*, 2025, **14**, 147.
11 P. M. Anandarajah, K. Shi, J. O. Carroll, A. Kaszubowska, R. Phelan, L. P. Barry, A. D. Ellis, P. Perry, D. Reid, B. Kelly and J. O'Gorman, *Opt. Express*, 2009, **17**, 12668–12677.
12 P. M. Anandarajah, *IEEE Photonics J.*, 2011, **3**, 112–122.
13 S. Shao, J. Li, H. Chen, S. Yang and M. Chen, *IEEE Photonics J.*, 2022, **14**, 1–6.
14 S. P. Ó Dúill, R. Zhou, P. M. Anandarajah and L. P. Barry, *IEEE J. Quantum Electron.*, 2015, **51**, 1–8.
15 Y. N. Li, L. Fan, G. Q. Xia and Z. M. Wu, *IEEE Photonics J.*, 2017, **9**, 1–7.
16 A. Quirce, *IEEE Photonics J.*, 2020, **12**, 1–14.
17 E. K. Lau, L. J. Wong and M. C. Wu, *IEEE J. Sel. Top. Quantum Electron.*, 2009, **15**, 618–633.
18 Y. T. Dai, X. F. Chen, L. Xia, Y. J. Zhang and S. Z. Xie, *Opt. Lett.*, 2004, **29**, 1333.
19 Y. T. Dai and J. P. Yao, *IEEE J. Quantum Electron.*, 2008, **44**, 938.
20 J. S. Li, H. Wang, X. F. Chen, Z. W. Yin, Y. C. Shi, Y. Q. Lu, Y. T. Dai and H. L. Zhu, *Opt. Express*, 2009, **17**, 5240–5245.
21 L. M. Zhang, S. F. Yu, M. C. Nowell, D. D. Marcenac, J. E. Carroll and R. G. S. Plumb, *IEEE J. Quantum Electron.*, 1994, **30**, 1389–1395.
22 B. S. Kim, Y. C. Chung and J. S. Lee, *IEEE J. Quantum Electron.*, 2000, **36**, 787–794.
23 Y. S. Zhang, L. Y. Li, Y. T. Zhou, G. W. Zhao, Y. C. Shi, J. L. Zheng, Z. K. Zhang, Y. Liu, L. J. Zou, Y. K. Zhou, Y. C. Du and X. F. Chen, *Opt. Express*, 2017, **25**, 27595–27608.

© 2025 The Author(s). Published by the Royal Society of Chemistry